https://doi.org/10.5194/egusphere-2026-3771
Preprint. Discussion started: 27 July 2026

Plume Emission Rate Estimation using Gaussian Plumes in Remote Imaging Spectroscopy with SPIIRE

Jay E. Fahlen[1], Philip G. Brodrick[1], David R. Thompson[1], Andrew K. Thorpe[1], and Robert O. Green[1]
Jet Propulsion Laboratory, California Institute of Technology 4800 Oak Grove Drive, Pasadena, CA 91109
Correspondence: Jay E. Fahlen (jay.e.fahlen@jpl.nasa.gov)

Abstract. The detection and quantification of methane and other trace gas emissions using remote sensing with imaging spectroscopy is an increasingly important tool for understanding local, regional, and global emissions. Traditional algorithms for quantifying the emission rate often rely on user-determined, instrument-dependent parameters and arbitrary plume boundaries. In this paper we present a new algorithm to estimate the emission rate based on a statistical inversion of a physical plume model that does not depend on such parameter choices or plume boundaries, termed SPIIRE. The method fully exploits instrument noise models, incorporates surface-albedo and atmospheric effects present in gas enhancement imagery, and is well suited for operational use. We present simulation results showing improved noise resilience, demonstrate performance against controlled-release experimental data using AVIRIS-3 and EMIT, and provide multiple examples using EMIT. We then show how the model can be extended to complex scenes having overlapping plumes and to spatially-distributed sources like landfills.

1 Introduction

In recent years, there has been tremendous progress in the detection and quantification of methane and other trace gas emissions through airborne and spaceborne imaging spectroscopy. This evolution has transitioned from initial demonstrations (Thorpe et al., 2013; Thompson et al., 2016) to robust monitoring capabilities (Cusworth et al., 2024; Zhang et al., 2025) within just a decade. These advancements have spurred the development of capabilities for existing missions, exemplified by NASA's Earth Surface Mineral Dust Source Investigation (EMIT) (Thorpe et al., 2025), and have led to the creation of innovative orbital instruments such as the Carbon Mapper Coalition Tanager-1 (Duren et al., 2025). Additionally, ongoing and completed controlled gas release experiments (Thorpe et al., 2021; Ayasse et al., 2023; Brandt et al., 2026) have demonstrated the ability of these technologies for quantifying emissions.

Traditional emission rate quantification methods applied to gas enhancement imagery typically assume constant emission rates and constant, spatially uniform wind. These assumptions imply that the total mass flux of gas remains constant across any cross-wind slice of the atmosphere downwind of the emission source. Thus, the emission rate can be inferred by converting the estimated gas enhancement for each pixel into mass enhancement, summing all pixels within the plume to create the Integrated Mass Enhancement (IME), and subsequently multiplying by the wind speed over the plume length. This results in the estimated emission rate in mass emitted per unit time (Thorpe et al., 2023; Varon et al., 2018; Duren et al., 2019; Brodrick et al., 2026;

https://doi.org/10.5194/egusphere-2026-3771
Preprint. Discussion started: 27 July 2026

Varon et al., 2020; Irakulis-Loitxate et al., 2021; Guanter et al., 2021; Sánchez-García et al., 2022; Roger et al., 2024; Kim et al., 2025; Li et al., 2026).

However, significant challenges persist in determining which pixels should contribute to the IME and how to accurately measure plume length. Plume boundaries are often defined through a combination of human input and basic image processing techniques, leading to variability in emission estimates based on subjective decisions. For example, Brodrick et al. (2026) uses the predetermined plume origin to seed a threshold-and-refine algorithm to identify a plume mask for the IME. Plume length can be calculated in a variety of ways, ranging from the longest dimension of the plume mask (Brodrick et al., 2026) to the square root of the mask area (Varon et al., 2018). Some authors choose to compensate for potential errors in the plume length measurement using an “effective" wind speed in which the wind speed is modeled as a parameterized function that is fit to either simulation results or experimental data. Consequently, IME-based methods frequently depend on tuned parameters that can significantly influence emission estimates and may require adjustments for different instruments, platforms (such as airborne versus spaceborne), or environmental conditions. Although these parameters can be and have been tuned using experimental data, the challenge of acquiring such data for orbital systems, along with the calibration process itself, remains a fundamental issue for traditional IME-based approaches.

Gaussian plumes have been extensively utilized in the literature for both plume modeling and emission rate estimation. The derivation typically assumes a point source emitting into a constant wind, yet turbulent diffusion effects are often incorporated by treating the downwind Gaussian width as a parameterized function of distance. Historically, the determination of these width parameters has relied on estimates of the atmospheric state, as detailed by Seinfeld and Pandis (2016), who derive Gaussian plumes and present various turbulent spreading models. Notable examples of emission rate estimation using Gaussian plumes include Krings et al. (2011), who analyzed overhead airborne data with multiple narrow passes through individual plumes, and Shah et al. (2019), who employed multiple vertical and horizontal samples at a single downwind location. Three recent studies—Nassar et al. (2021), Kuhlmann et al. (2024), and Pang et al. (2025)—adapt Gaussian plumes to gas enhancement imagery, each differing in their methodologies. While none of these studies employ a probabilistic framework, Kuhlmann adapts the spreading parameters to the data and utilizes a flexible plume. In contrast, both Nassar and Pang use straight plumes with fixed spreading parameters, with Nassar's based on wind speed (see Section 2.2 of Nassar et al. (2021)).

In this paper, we present a Maximum Likelihood Estimation (MLE) method for emission rate estimation utilizing Gaussian plume models (Seinfeld and Pandis, 2016; Varon et al., 2018) called Statistical Plume Imaging Inversion for Rate Estimation, SPIIRE. Our approach estimates parameters directly from the data, comparing the plume model to the observed gas enhancement imagery to assess the likelihood that the measured data represents a noisy realization of a Gaussian plume. A numerical optimizer determines the parameters that maximize this likelihood, or equivalently, minimize the weighted model-data error, resulting in a more objective estimation of emission rates. This method adapts a physical plume model to observational data, demonstrating robustness against instrument noise and surface albedo effects, while minimizing reliance on user-specific or instrument-specific parameters.

SPIIRE incorporates three key features that collectively ensure highly accurate model fits. First, it estimates all parameters within a turbulent Gaussian plume model directly from the data, including those related to downwind spreading. Second, the

https://doi.org/10.5194/egusphere-2026-3771
Preprint. Discussion started: 27 July 2026

Gaussian plume is designed to be flexible in the cross-wind direction, allowing it to adapt to the observed plume as it aligns with local topography and variations in wind velocity. Lastly, the probabilistic MLE framework takes into account variable detection sensitivity caused by local atmospheric and surface albedo effects, downweighting noisy, low-signal pixels during optimization based on their known uncertainties (Fahlen et al., 2024). Together, these enhancements yield quantitatively precise models of observed plumes while minimizing the subjectivity associated with manual plume delineation.

More complex scenarios that challenge traditional IME-based approaches include plume complexes (Duren et al., 2019; Sánchez-García et al., 2022; Thorpe et al., 2023) and area sources (Cusworth et al., 2024; Maasakkers et al., 2022; Zhang et al., 2025; Marjani et al., 2024). Plume complexes consist of multiple apparent sources whose plumes merge or overlap, complicating the ability of IME-based methods to discern which gas enhancements should be attributed to each source. This overlap can also obscure the identification of plume length, potentially introducing significant errors. Pang et al. (2025) propose a novel approach for estimating emissions from plume complexes by employing a Gaussian plume inversion to "separate" overlapping plumes, allowing an IME-based strategy to be applied to each plume individually. Area sources, such as landfills, emit gas over a relatively large and contiguous area, often lacking a distinct downwind tail. These sources frequently do not meet the assumptions inherent in IME-based methods, resulting in diminished accuracy.

The Gaussian plume model can effectively address these challenges by simultaneously modeling multiple plumes. Overlapping plumes can be easily accommodated by summing the concentrations of multiple Gaussian plumes and optimizing each plume's parameters concurrently. Area sources can similarly be represented by clustering several Gaussian plumes within a small region surrounding the source and optimizing their parameters to ensure that the combined forward model accurately reflects the observed enhancement. These generalizations of the Gaussian plume model are shown to provide excellent fits to observed data.

The paper is organized as follows: Section 2 details the 2D Gaussian plume inversion method, including a derivation of the traditional IME method as a simplification of the 2D plume model. Section 3 presents a comparison of the two methods using simulated plumes injected into real data, followed by a validation using methane controlled release data from the airborne AVIRIS-3 instrument (Coleman et al., 2026). In Section 4 we demonstrate the value of plume modeling for EMIT (Green et al., 2023) methane enhancement data (Brodrick et al., 2026), including overlapping plume complexes and area sources, followed by conclusions and further discussion.

2 Plume Model Inversion

2.1 Gaussian Plume Models

A simple model for the concentration C of a gas emitted from a point source and carried in the wind is the Gaussian plume model, defined by

$$C(x,y,z) = \frac{Q}{u}\frac{1}{\sqrt{2\pi}\sigma_y}e^{-\frac{y^2}{2\sigma_y^2}}\frac{1}{\sqrt{2\pi}\sigma_z}e^{-\frac{z^2}{2\sigma_z^2}}, \tag{1}$$

https://doi.org/10.5194/egusphere-2026-3771
Preprint. Discussion started: 27 July 2026

where (x, y, z) is a right-handed coordinate system with positive z normal to the Earth's surface and x increasing in the direction of the wind speed vector which was assumed constant in space and time in Eq. 1's derivation (Seinfeld and Pandis, 2016). The plume origin is assumed to be at $(x, y) = (0, 0)$. It is common to assume the plume originates at some positive z, but for our purposes we will neglect this as will become clear shortly. The quantity Q is the gas emission rate, typically in units of kilograms per hour, and u is the wind speed.

The plume spreading parameters are denoted by σ_y and σ_z and are generally functions of the downwind position x. A variety of spreading models and parameterizations exist for Gaussian plume models (Carrascal et al., 1993). A particularly common model is to assume that

$$\sigma_y(x) = a\left(\frac{x}{d}\right)^b. \tag{2}$$

Different authors find different values for parameters a, b, and d and often recommend that they change with wind speed or atmospheric state (Pasquill-Gifford, for example, Seinfeld and Pandis (2016)). In this work, we take $d = 1000$ m and allow the fitting procedure described below to find the values of a and b that best match the data. Importantly, the spreading model does not include an explicit dependence on the wind speed. This means that the wind speed only appears in the ratio Q/u. As a result we cannot estimate Q separately from u, but only their ratio, which we call C_Q below. For convenience, we use units of kg/hr per m/s for C_Q as Q is typically kg/hr while u is m/s.

2.2 Maximum Likelihood Estimation of Emission Rate

We seek to estimate C_Q by comparing the Gaussian plume model with the remote measurement of the concentration length $\hat{l}_{i,j}$, where i, j are spatial pixel indices. This requires adapting the 3D model to the 2D the measurement at hand by integrating over the z direction, giving the 2D Gaussian model

$$C_{2D}(x, y) = \frac{Q}{u}\frac{1}{\sqrt{2\pi}\sigma_y}e^{-\frac{y^2}{2\sigma_y^2}}. \tag{3}$$

Unfortunately, the data are noisy, so we seek a probabilistic model for the measurement following Fahlen et al. (2024). Treating each pixel as a realization from a normal distribution with mean given by the 2D plume model and variance equal to the pixel uncertainty, we obtain the probability distribution function

$$p_{C_{2D}}(\hat{l}_{i,j}) = \frac{1}{\sqrt{2\pi S_{i,j}^2 U_{i,j}^2}}e^{-\frac{(\hat{l}_{i,j} - 2kS_{i,j}C_{2D}(x_i, y_j))^2}{2S_{i,j}^2 U_{i,j}^2}}, \tag{4}$$

where $S_{i,j}$ and $U_{i,j}$ are the sensitivity and uncertainty, respectively, at pixel (i, j). In this case we use the "uncorrected" uncertainty SU because we choose to use the measurement $\hat{l}$ without the sensitivity correction (Fahlen et al., 2024; Brodrick et al., 2026). This is more style than substance though as the S could just as easily be factored out of the exponent leaving the "corrected" concentration length instead. The factor k, which converts the model from area concentration [kg/m^2] to concentration length [ppm m], is 10^6 (m^3/mol) (mol/kg). In the rest of this paper, we consider methane plumes near the surface at standard temperature and pressure (STP), yielding $k \approx 1.4 \times 10^6$ ppm m^3 / kg. The factor of 2 in the exponent's numerator is

https://doi.org/10.5194/egusphere-2026-3771
Preprint. Discussion started: 27 July 2026

to account for the light's path through the plume. Although this factor in principle depends on the look and solar angles along with the plume's cross-sectional shape and height above the ground, we assume that the concentration length measurement in each pixel represents a double path through the plume: down from the sun then back up from the ground.

To estimate C_Q, we form the likelihood of the plume model parameters $\theta \in \Theta$ given the data, given by

$$\Lambda(\theta) = \prod_{i,j \in P} p_{C_{2D}}(\hat{l}_{i,j};\theta), \tag{5}$$

and then seek the values of those parameters that maximize the likelihood, as in

$$\hat{\theta} = \underset{\theta \in \Theta}{\arg\max}\, \Lambda(\theta). \tag{6}$$

The product in Eq. 5 is taken over all spatial pixels inside the plume boundary P or over the rectangular region that bounds the manually-determined plume boundary plus a buffer region. In the results below, we use the buffer method with a size of 10 pixels. The advantage of including pixels beyond the manual delineation is twofold. First, we eliminate the subjectivity necessarily associated with drawing a boundary around the apparent plume by allowing the optimization to determine the plume shape without arbitrary restrictions. Second, we allow the method to take advantage of the region of gas enhancement that falls below the per-pixel noise threshold past the end of the plume. Although not visibly associated with the plume and therefore not included in the manual delineation, the model predicts gas enhancement here and its presence can be exploited by the likelihood formulation. The parameter space Θ includes, among other variables discussed below, the emission rate C_Q and the spreading parameters a and b, but also a rotation α about the plume origin to allow for arbitrary wind directions. Because the Gaussian plume model is derived for *point* sources, the concentration becomes infinite at the origin as the spreading model shrinks. In the implementation here, we work around this problem by forcing the origin to always lie on a pixel boundary that is excluded from P. However, a different spreading model σ_y or, ideally, a more physical plume model based on a finite-sized gas vent, could achieve a similar effect.

The plume model in Eq. 3 assumes constant wind, but we can accommodate some wind direction variation by allowing the cross wind mean to vary as a function of the downwind position, as in $C_{2D}(x,y) \rightarrow C_{2D}(x,y-m(x))$. This is done by parameterizing $m(x)$ and adding those parameters to Θ. In the current implementation, m is broken into separate parameters m_v spaced at 3 times the Ground Sampling Distance (GSD) in the along wind x-direction. Previous work with Gaussian plumes has allowed wind variation using Bezier curves (Kuhlmann et al., 2024), but we have found that the choice of using 3 times the GSD rather than just the GSD works well for the relatively high-spatial-resolution data used below. We have found that the emission estimate is not very sensitive to this choice while the adapted plume models are more visually consistent. The number of m_x parameters is the number that fit from the plume origin to the far end of the retrieval region.

We use the SciPyBoundedMinimize optimizer provided in the jaxopt python library (Blondel et al., 2021). The initial value for the wind direction is computed as the line from the manually-determined plume origin to the centroid of the plume boundary. In summary, the likelihood function in Eq. 5 is optimized over C_Q, a, b, α, and the set of m_x parameters. In practice, we have found that using the log likelihood and estimating $\ln C_Q$ and $\ln a$ improves the reliability of the optimizer.

https://doi.org/10.5194/egusphere-2026-3771
Preprint. Discussion started: 27 July 2026

The uncertainty in the emission rate Q depends on many factors, including instrument noise and wind speed. These two can be combined using standard error propagation methods based on the expression $Q = uC_Q$, yielding

$$\sigma_Q^2 = \left(\sigma_{C_Q}\frac{\partial Q}{\partial C_Q}\right)^2 + \left(\sigma_u \frac{\partial Q}{\partial u}\right)^2. \tag{7}$$

We calculate σ_{C_Q} using the Cramer-Rao bound (Van Trees, 2004) and σ_u as the standard deviation of the surrounding wind samples following Brodrick et al. (2026). Another source of error is due to the mismatch between the true plume and the Gaussian model, but this is difficult to quantify. The use of the sensitivity and the m_v help to reduce this error, but the uncertainty persists, meaning that the above expression for uncertainty likely underestimates the true uncertainty.

2.3 Traditional Integrated Mass Enhancement

The traditional (IME) method (Thorpe et al., 2023; Varon et al., 2018; Brodrick et al., 2026) can be put into a likelihood-based formulation too, which we briefly show here as a way to contrast the probabilistic framework above with the forced preprocessing of IME methods. Integrating Eq. 3 in the cross wind direction yields the 1D plume model

$$C_{1D}(x,y) = \frac{Q}{u}. \tag{8}$$

This cannot be compared against the data without first similarly summing the overhead gas enhancement imagery. This arbitrary preprocessing step is not dictated by the likelihood formulation. Traditionally, the calculation of IME is done using a simple threshold-and-refine method that must decide in advance which pixels belong to the plume and which do not. One must also decide how to include negative gas enhancements, which naturally occur in matched-filter-based detection algorithms, and how to incorporate bias correction or per-pixel uncertainty estimates (Fahlen et al., 2024). Various authors have chosen various methods for this cross-wind sum, but for our purpose, we simply assume that it has been done somehow so that we can compare the model against the data to obtain the log-likelihood function given by

$$\lambda_{1D} = \sum_{i \in P}\left(\hat{l}_i - 2k_{1D}\frac{Q}{u}\right)^2. \tag{9}$$

In this case, P is the set of along-wind pixels that have been summed cross wind to yield the 1D concentration length $\hat{l}_i$. The constant k_{1D} converts the line concentration [kg/m^2] to concentration length. Assuming the set of pixels in P is determined by the fetch length and summing all N along-wind pixels from the origin to the fetch length f, we can find the maximum of Eq. 9 to yield the maximum likelihood 1D emission rate given by

$$\hat{Q}_{1D} = \frac{u}{2k_{1D}f}\sum_{i=0}^{N-1}\hat{l}_i. \tag{10}$$

In the remainder of this paper, we define the “Simple IME" method to follow Brodrick et al. (2026), although we note that the specific implementation and choice of parameters used in traditional IME methods can generate significant variability in the estimates. Indeed, the lack of such parameters is a major advantage of the present method. Below, we compare Simple IME against SPIIRE to demonstrate how the ad-hoc preprocessing steps required by Simple IME introduce additional noise.

https://doi.org/10.5194/egusphere-2026-3771
Preprint. Discussion started: 27 July 2026

3 Results

We demonstrate SPIIRE using both airborne AVIRIS-3 (Coleman et al., 2026) and space-borne EMIT (Green et al., 2023) methane enhancement data (Brodrick et al., 2026). Although we use methane emissions throughout as a test case, we note that the method could apply equally well to other gases or even to aerosol plumes. Both instruments are pushbroom imaging spectrometers with a spectral range of approximately 380-2500 nm and 7 nm spectral resolution. EMIT's swath width is approximately 80 km with 60 m spatial resolution. AVIRIS-3's equivalent, being an airborne sensor, is variable depending on the flight altitude but its spatial resolution ranges from approximately 0.5 to 6 m for the data used here. For both instruments, a column-by-column spectral matched filter is used on the calibrated radiance data to estimate the methane concentration length in each spatial pixel (Thorpe et al., 2017; Thompson et al., 2015) along with its sensitivity (bias) and uncertainty (Fahlen et al., 2024). The EMIT data can be found following Thorpe et al. (2025) and the AVIRIS-3 data following Chlus et al. (2024).

3.1 Simulated Data

To demonstrate SPIIRE's superior noise performance, we simulated 600 plumes using the 2D Gaussian plume model with random C_Q and spreading parameters but with no bends (the simulated m_x are all 0). We choose to simulate Gaussian plumes because they satisfy the assumptions of both methods. The simulated C_Q are uniformly distributed between 200 and 3000. The plumes are injected (added) into random locations in 263 randomly chosen EMIT methane enhancement scenes that have previously been determined to have no clouds or true emissions. We include the local sensitivity when injecting the simulated plume into the noisy data. Figure 1 shows the simulation results by comparing the Simple IME method on the left with SPIIRE on the right. As expected, SPIIRE has superior noise performance and is unbiased over the full range. We note that it may be difficult in practice to realize the full noise improvement as data-model mismatch will inevitably occur due to unmodeled effects like changing winds, local topography variation, intermittent sources, and so on. However, these effects often plague traditional IME-based methods too, making SPIIRE's noise resilience an important contribution.

3.2 Controlled Release Results

We demonstrate the accuracy of SPIIRE using controlled-release experimental data (Duren et al., 2025). Following the approach in El Abbadi et al. (2024), methane is released and accurately measured from a point 7.3 m above ground at two different sites: Casa Grande, AZ at (32.822°N, 111.785°W) and Evanston, WY at (41.275°N, 110.930°W). AVIRIS-3 performed 110 passes at Evanston on Sept. 11-14, 2024 and 34 passes at Casa Grande on Nov. 4-5, 2024. EMIT observed the site during 7 overpasses. Wind speeds and directions are measured at 2 and 10 meters above ground using a sonic anemometer.

An example plume is shown in Fig. 2 using AVIRIS-3 data from Nov. 4, 2024 at Casa Grande, Arizona (AV320241104t183250). The white dot and line are, respectively, the manually-determined plume origin and boundary. As mentioned previously, the retrieval region P includes all pixels in the rectangular region within 10 pixels of the widest part of the plume (all pixels shown in Fig. 3a). The adapted Gaussian plume model is shown in Fig. 3b with the sensitivity correction applied. The bending of the plume model to accommodate apparent wind direction changes in the plume is achieved through the m_x. A key feature of the

https://doi.org/10.5194/egusphere-2026-3771
Preprint. Discussion started: 27 July 2026

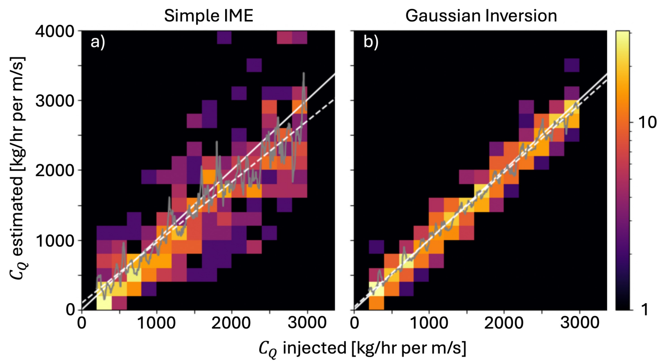

Figure 1. Histograms showing the estimated C_Q along the vertical axis and the injected C_Q along the horizontal for a) the Simple IME method and b) SPIIRE. The solid white line is the one-to-one line, the dashed white line is the linear regression, and the gray line is the moving average.

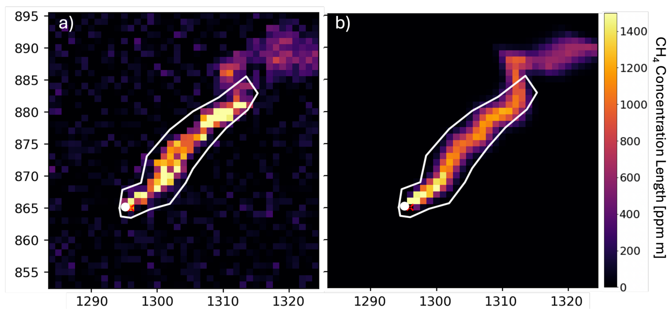

Figure 2. AVIRIS-3 SPIIRE example from the Nov. 4, 2024 controlled release experiment. Figure a) shows an image of estimated concentration length, and b) shows the fit 2D Gaussian model plume with sensitivity correction. The white dot and line are the manually identified plume origin and plume boundary. The metered emission rate is 155 kg/hr and the estimated rate is 165±27 kg/hr with an approximately 4 m/s wind speed. AV3 flightline AV320241104t183250.

method is the modification of the model by the sensitivity to account for surface- and atmospheric-related biases, although this effect is modest at the mostly-uniform experimental site.

The emission rates from SPIIRE are plotted against the metered emission rate for the two AVIRIS-3 controlled release experiments (Duren et al., 2025) in Fig. 3. We have removed several overpasses where the plumes are too weak to be credibly detected. The linear fit is shown in dashed gray with the fit statistics inset. The wind speeds used are from the 2 meter sonic anemometer. Both the wind speeds and the metered emission rates are the mean over the preceding 30 seconds relative to the overpass time. For both experimental locations, the estimated emission rates are accurate in the aggregate with a reasonable spread about the true emission rate. The Simple IME method yields similar but slightly worse performance, driven in part by outliers whose estimates are sensitive to the particular choices of implementation and parameter. The slope for Simple IME at

https://doi.org/10.5194/egusphere-2026-3771
Preprint. Discussion started: 27 July 2026

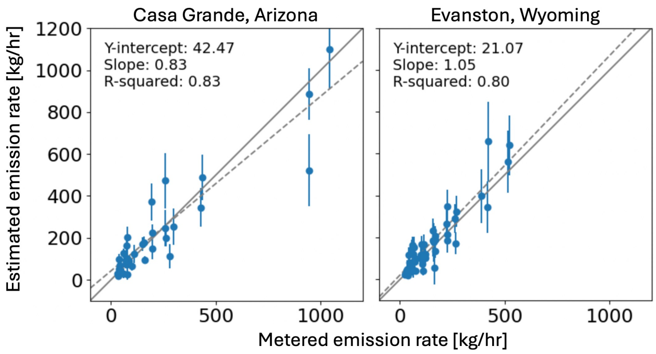

Figure 3. Emission rate estimates using SPIIRE on the AVIRIS-3 Arizona (left) and Wyoming (right) controlled release experiment data collections. The one-to-one line is solid gray while dashed gray indicates the linear regression through all points. In calculating the emission rate, the wind speed from the 2 m tower was used after averaging over the preceding 30 s. We note that results vary depending on the choice of tower and smoothing period.

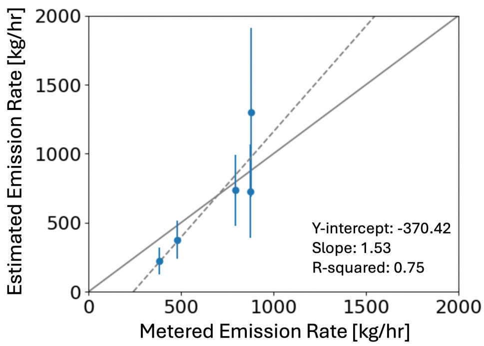

Figure 4. Emission rate estimates using SPIIRE on the EMIT Arizona controlled release experiment data collections. The one-to-one line is solid gray while dashed gray indicates the linear regression through all points. In calculating the emission rate, the wind speed from the 2 m tower was used after averaging over the preceding 30 s. We note that results vary depending on the choice of tower and smoothing period.

Wyoming is approximately 1.3 with an R-squared value of 0.69 while at Casa Grande we obtain a slope of 0.53 with R-squared of 0.72. We note that uncertainty in the wind speed and decisions about how it is processed affect the comparisons too.

The estimated emission rates for the EMIT controlled release experiment overpasses are shown in Fig. 4. EMIT did not detect the first two despite relatively large metered emission rates, likely due to high winds during those collections (5.1 and 5.2 m/s, respectively). We note that SPIIRE's performance may not be representative in this case because the plumes do not satisfy the steady-state assumption. Because the releases only started a few minutes before the overpass, they are short compared to typical plumes, all between 8 to 16 EMIT pixels (<1 km). This means that the assumptions guiding the decision to use a buffer region surrounding the visible plume do not hold here and we assume instead that the end of the apparent plume actually

https://doi.org/10.5194/egusphere-2026-3771
Preprint. Discussion started: 27 July 2026

represents the end of the true gas enhancement. Accordingly, we modified the cost function for the five examples shown in Fig. 4 to include only the pixels within a circular region surrounding the emission source and whose radius matches the last visible portion of the plume. This choice reduces the number of pixels used in the retrieval and likely degrades the performance relative to that observed in the AVIRIS-3 data in Fig. 3. Nevertheless, the estimator's performance is good, with four of the five points within their uncertainty of the metered emission rate.

We note that the Simple IME method used to produce the estimates quoted throughout this paper requires a different set of user-defined parameters for the AVIRIS-3 results versus the EMIT results. This is to address the differences in spatial resolution and noise performance between the two instruments. It is possible to tune these parameters for AVIRIS-3 using the controlled release data, but the limited availability of such data for EMIT means that it is difficult to project the Simple IME performance quoted above to EMIT observations. In contrast, the SPIIRE results throughout this work use the same set of parameters for both instruments, meaning that the validation shown here using AVIRIS-3 and EMIT controlled release data is more likely to apply to the full EMIT database.

3.3 Plume Modeling and Interpretation

A major benefit of SPIIRE is the improved understanding of visually-complex plumes. Figure 5 and the third example in Fig. 6 exhibit EMIT plumes whose initial appearance suggests an intermittent source or turbulent winds. Instead, the 2D Gaussian plume model adapted to the data and combined with the sensitivity indicates that the emission source is constant in time, with the apparent intermittency caused by background albedo effects captured by the sensitivity. The cross-wind transects on the right side of the Fig. 5 demonstrate the quality of the plume modelling in this case. Although no ground truth emission rate is available for this plume, SPIIRE estimated C_Q at 3.4 times that of the Simple IME method. This plume provides an example of the two methods diverging despite the plume appearing to be due to a point emission source. In this case the model-data agreement is excellent, suggesting SPIIRE's estimate is likely a more accurate representation of the true emission rate.

4 Applications

4.1 Isolated Plumes

Traditional IME-based methods are currently being used operationally and their emissions estimates are publicly available, including for example Duren et al. (2025); Thorpe et al. (2025), subject to quality control thresholds (Brodrick et al., 2026; Cusworth et al., 2024). SPIIRE could be readily incorporated into such workflows to augment the estimates and to provide the additional benefits of plume interpretation using the adapted 2D Gaussian model. As described in the following subsections, SPIIRE may also help to relieve the quality control thresholds by providing a new method to quantify otherwise challenging plumes in difficult environments. Three more SPIIRE examples from the EMIT database are shown in Fig. 6.

https://doi.org/10.5194/egusphere-2026-3771
Preprint. Discussion started: 27 July 2026

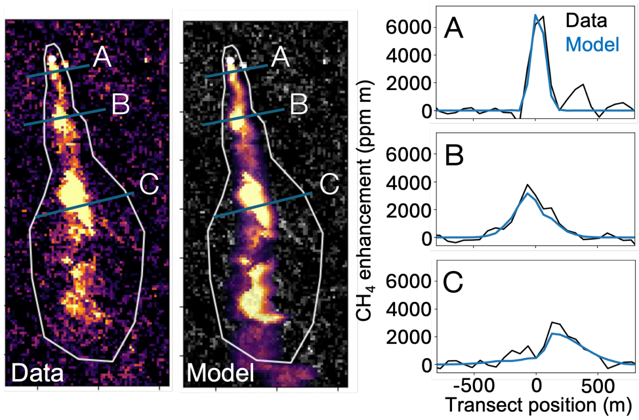

Figure 5. SPIIRE example from EMIT CH4_PlumeComplex-2794 from Feb. 28, 2024 at 27.9686°N latitude and 69.8097°E longitude in Pakistan. From left to right: data image of estimated concentration length, fit 2D Gaussian model plume with sensitivity correction (color) overlaid on data (grayscale), and plots of three transects showing the data and the sensitivity-corrected model. The white dot and line are the manually identified plume origin and plume boundary, and the color scale is the same as that in Fig. 2. The Simple IME emission rate estimate is 6997±784 and the SPIIRE estimate is 9295±1000 kg/hr.

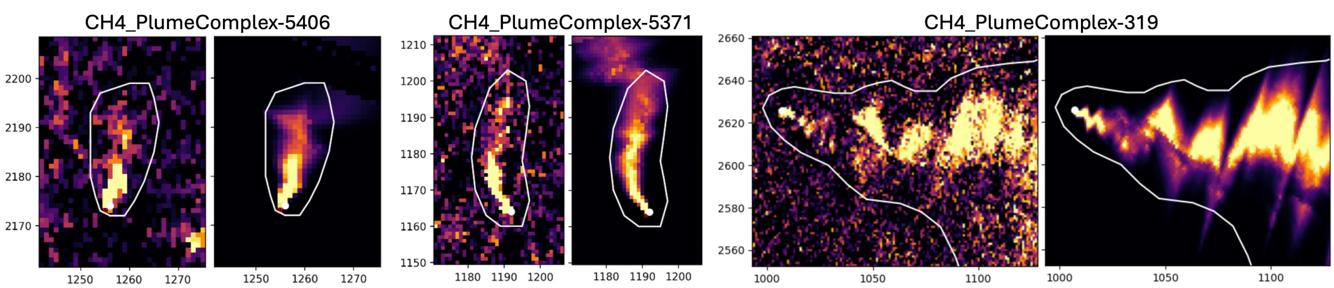

Figure 6. SPIIRE examples from EMIT plotted as in Fig. 2, left to right: CH4_PlumeComplex-5406 from 6/2/2025 at (49.490°N, 35.697°E), CH4_PlumeComplex-5371 from 7/17/2025 at (-21.968°N, 148.024°E), and CH4_PlumeComplex-319 from 6/12/2023 at (41.437°N, -111.169°E). All three are likely oil and gas facilities. The Simple IME estimates, left to right, are 1148±65, 5619±290, and 10589±874 kh/hr, and the corresponding SPIIRE estimates are 1793±101, 4596±247, and 21736±1559 kg/hr.

https://doi.org/10.5194/egusphere-2026-3771
Preprint. Discussion started: 27 July 2026

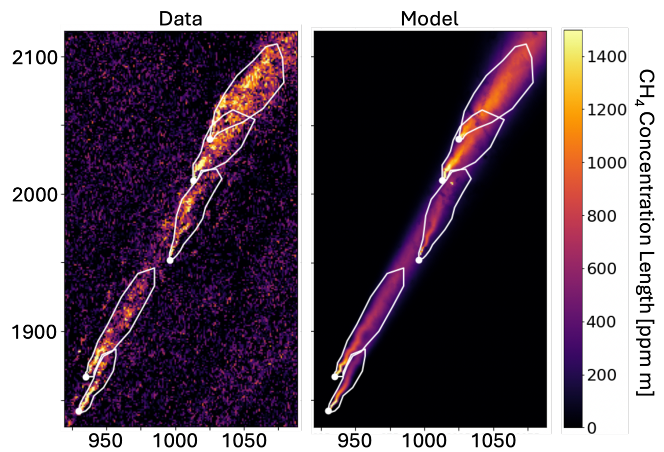

Figure 7. SPIIRE example from EMIT CH4_PlumeComplex-4191 from Feb. 1, 2025 at 35.3551°N latitude and 40.3505°E longitude, likely an oil and gas site. The left plot shows the measured CH4 enhancement and the right the fit 2D Gaussian model. The white dot and line are the manually identified plume origins and plume boundaries. Note that the boundaries are only shown for convenience, they are not used in the inversion except to determine the plume bounding box.

4.2 Overlapping Plume Complexes

Traditional IME-based approaches to plume emission rate estimation do not perform well in plume complexes having multiple apparent sources whose plumes merge downwind. In such cases it is impossible to know how to allocate CH4 enhancement pixels to any particular source. However, it is straightforward to adapt SPIIRE to plume complexes by simultaneously inverting multiple plumes, with the model to be optimized simply the sum of each plume. Figure 7 shows an example EMIT scene having multiple apparent sources. Originally labeled CH4_PlumeComplex_4191, it is clear from a close examination of the data image at left along with high resolution base-layer imagery from Google Maps that there are in fact several point sources. The wind direction in this case appears to be coincidentally aligned so that the plumes overlap. We identify five independent point sources and simultaneously invert five corresponding Gaussian plumes. It is not necessary to assign the CH4 enhancement in a particular pixel to any particular plume as the simultaneous inversion automatically adapts each plume to the data to provide a combined CH4 model over the entire set of pixels in the figure. We note that the manual plume delineations shown in white are not used in the inversion are are only provided as a visualization.

4.3 Distributed Sources

Distributed, or area, sources are also challenging for IME-based quantification methods as they often do not appear to satisfy the assumptions needed to calculate the emission rate based on their IME. In particular, these sources often appear as amorphous enhancement regions spanning many pixels but without any apparent point source or long downwind tail. The plume in Fig. 8, showing a landfill in northwest China, is a good example. Using the Gaussian plume, we can model distributed sources

https://doi.org/10.5194/egusphere-2026-3771
Preprint. Discussion started: 27 July 2026

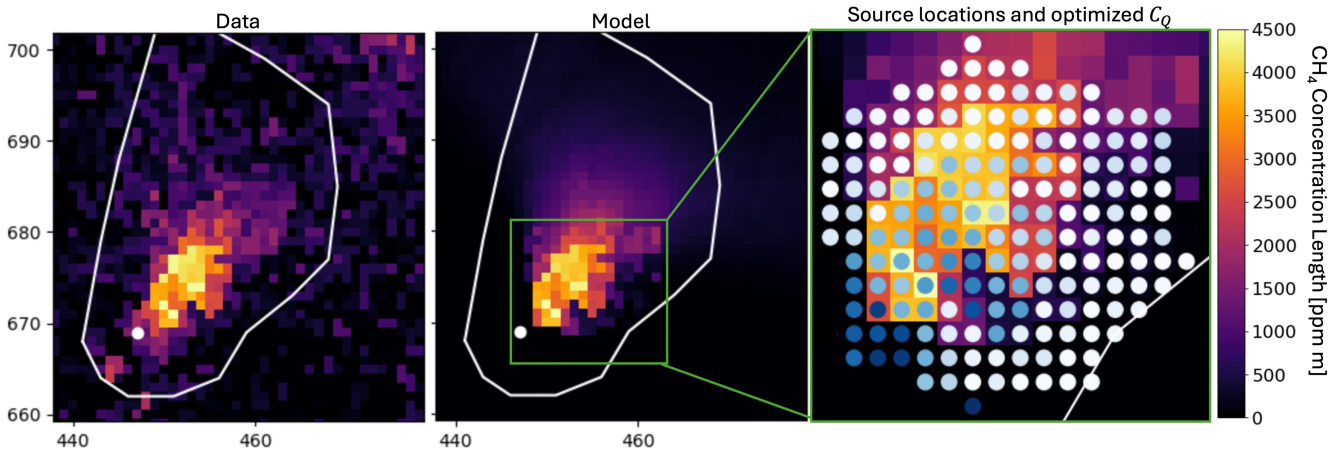

Figure 8. SPIIRE example from EMIT CH4_PlumeComplex-508 from Aug. 18, 2022 at a landfill at 44.0395°N latitude and 87.8681°E longitude. The left plot shows the measured CH4 enhancement and the middle the fit 2D Gaussian model with sensitivity correction. This plume is due to a landfill whose emissions are spread over several EMIT pixels. The right image shows the location of each point source in the model, with color indicating relative source strength: white represents no emission while dark blue is the maximum. The optimizer found that most sources have little or no emission. The combined emission rate is estimated to be approximately 11000 kg/hr with a wind speed of 3.3 m/s.

as a collection of point sources spread over a predefined area and then allow the optimizer to individually determine each plume's C_Q. We assume that the wind speed is the same over the entire region, so we force each point plume to share the same spreading parameters. In the example shown in Fig. 8, we selected a polygon that covers the landfill and surrounding area using high-resolution Google Maps imagery. This region is approximately 800 m wide. The point sources within the polygon, one per pixel, are shown in the green inset on the right side of the figure with color indicating relative intensity. Specifically, white represents no emission and dark blue relatively high emission. The resulting optimized model is shown in the middle panel of Fig. 8. Intriguingly, the optimizer found that the data is best represented by a relatively few sources concentrated near the bottom left and middle of the enhancement region. The lack of downwind tail, a common feature of distributed sources, is also modeled well using the collection of point sources. The simple IME method yields an estimated emission rate of approximately 6200 kg/hr with a wind speed of 3.3 m/s while the distributed point source model yields approximately 11,000 kg/hr. The true emission rate is not known, but the excellent data-model agreement shown in Fig. 8 suggests the higher number may be more accurate.

5 Discussion

SPIIRE's accuracy on the experimental data shown in Figs. 3 and 4 suggests that the method could be operationalized to other gases and even aerosol plumes. We have performed the inversion using a single point source plume on the majority of the EMIT

https://doi.org/10.5194/egusphere-2026-3771
Preprint. Discussion started: 27 July 2026

methane plume database with generally robust results provided the plumes satisfy the point source assumption. Following the quality control methods already in use (Cusworth et al., 2024; Brodrick et al., 2026), SPIIRE could directly augment traditional IME estimates and be readily adapted to any type of emission, ranging from other gases (CO, NH_3, *etc.*) to aerosol plumes due to, for example, wildfires. For the many plumes that do not meet the point source assumption, the overlapping and area source models demonstrated in Section 4 present a path forward. More work is needed to use these operationally, however, especially in determining how many sources to use and where to put them. The example shown in Fig. 7 was relatively easy to manually identify the various sources, but this is often not the case, nor is manual identification a viable long-term solution. One potential path is suggested by the observation that the optimizer successfully avoided adding extraneous plumes in Fig. 8, suggesting that plumes could be seeded automatically at local maxima in the enhancement with the optimizer free to allocate source strengths. Alternatively, the distributed source model could be used for all plumes, although care must be taken to avoid increasing the dimensionality of the optimizer beyond what can be reasonably solved.

Apart from improvements in measurement precision, a major advantage of SPIIRE is that it alleviates the need for subjective plume boundaries. Even where workflows use automated ML-based plume segmentation to speed labeling, these systems are generally trained on human-labeled data and thus subject to the same human biases in the plume definition. In contrast, the 2D model is defined over an infinite geographic area, removing the boundary as a source of error. Only the plume origin need be identified. Thus, it would only require an automated system capable of finding plume origins to enable a fully automatic, end-to-end plume quantification capable of handling the enormous data volumes of next generation imaging spectrometers.

The advantages of the adapted plume model also include better knowledge of and resilience to turbulent wind effects that can distort the observed plume shapes and degrade the accuracy of traditional IME-based approaches (Gałkowski et al., 2025). Although there is no doubt that turbulent winds can cause plumes to appear bunched up, Fig. 5 shows that in many cases what appear to be turbulent wind effects are in fact measurement artifacts that can be corrected in the retrieval. Additionally, SPIIRE is likely less sensitive to turbulent wind effects when they do occur for two reasons. To understand why, imagine a constantly-emitting source with small gas clouds that exceed the concentration predicted by a Gaussian plume model in some parts of the plume. Conservation of mass through the plume means that the excesses must also be accompanied by “holes" elsewhere. The algorithms that detect pixels to include in the IME calculation may fail to incorporate these holes, leading to a mismatch in the IME and fetch length and thus to errors in the emission rate estimate. SPIIRE, in contrast, fits the model through the gas clouds and holes, an averaging effect that smooths over the turbulence.

5.1 Wind Speed Estimation

A major challenge with emission rate quantification is in the estimation of the wind speed. Historically the wind speed has been derived from weather reanalysis data, like HRRR (Dowell et al., 2022) and ERA5 (Hersbach et al., 2020), but recent work using multiple observations separated by a few seconds provides an alternative based on the observation itself (Eastwood et al., 2025). A seemingly straightforward improvement to the method described above would be to simply simultaneously estimate the wind speed along with the other parameters, but, as mentioned in Section 2, the functional form of the standard plume model in Eq. 3 is degenerate in Q and u. Pang et al. (2025) attempt this, which may partially explain the poor performance

https://doi.org/10.5194/egusphere-2026-3771
Preprint. Discussion started: 27 July 2026

that they obtained in their Gaussian plume inversions. Alternative models with more explicit dependence on wind speed exist, as in Eq. 4 of Kuhlmann et al. (2024), but these either have other degeneracies or are apparently nonphysical. We have not been able to generate meaningful results with them. We have also considered establishing a correlation between the retrieved spreading parameters a and b with the various studies that predict them using atmospheric stability classes (Pasquill-Gifford, for example, as in Seinfeld and Pandis (2016); Carrascal et al. (1993)). Unfortunately, the retrieved values for these parameters often exceed their published ranges making the correlation difficult to establish. We therefore leave simultaneous wind speed estimation for future work, especially the development of a physical plume model with explicit wind speed dependence that cannot be compensated by a nuisance parameter.

6 Conclusions

SPIIRE addresses key challenges in the field, including the subjective delineation of plume boundaries and the reliance on hard-to-determine parameters. By integrating a probabilistic framework, we enhance the reliability of emission rate estimations, allowing for better adaptation to real-world conditions. Moreover, the model's flexibility enables it to accommodate complex scenes with overlapping plumes and spatially distributed sources, providing a more comprehensive understanding of emission dynamics.

In summary, this paper aims to bridge the gap between traditional methodologies and modern requirements for emission quantification, offering a robust, flexible, and user-independent approach. We demonstrate the effectiveness of our method through simulation results, controlled-release experimental data, and practical applications using different imaging spectrometers, highlighting its potential for widespread operational use in environmental monitoring. Additionally, the algorithm can be extended to estimate emission rates in complex scenarios involving multiple overlapping plumes and distributed sources, such as landfills.

Data availability. The EMIT data used in the work is available following Thorpe et al. (2025) and the AVIRIS-3 data following Chlus et al. (2024)

Author contributions. JF designed and performed the study and drafted the manuscript; PG and DT assisted with research methodology and analysis and manuscript drafting; AT assisted with research methodology, critical revision, and project supervision; RG supervised the project.

Competing interests. There are no competing interests.

https://doi.org/10.5194/egusphere-2026-3771
Preprint. Discussion started: 27 July 2026

Acknowledgements. The research was carried out at the Jet Propulsion Laboratory, California Institute of Technology, under a contract with the National Aeronautics and Space Administration (80NM0018D0004). © 2026. California Institute of Technology. Government sponsorship acknowledged.

References

Ayasse, A. K., Cusworth, D., O'Neill, K., Fisk, J., Thorpe, A. K., and Duren, R.: Performance and sensitivity of column-wise and pixel-wise methane retrievals for imaging spectrometers, Atmospheric Measurement Techniques, 16, 6065–6074, https://doi.org/10.5194/amt-16-6065-2023, 2023.

Blondel, M., Berthet, Q., Cuturi, M., Frostig, R., Hoyer, S., Llinares-López, F., Pedregosa, F., and Vert, J.-P.: Efficient and Modular Implicit Differentiation, arXiv preprint arXiv:2105.15183, 2021.

Brandt, A., Reuland, F., Adams, T., Sherwin, E., Abbadi, S. E., and Kort, E.: Unlocking credible space-based methane sensing through a year-long single-blind test, https://doi.org/10.21203/rs.3.rs-9110475/v1, 2026.

Brodrick, P. G., Thorpe, A. K., Fahlen, J., and Thompson, D. R.: EMIT Greenhouse Gas Algorithms: Greenhouse Gas Point Source Mapping and Related Products, Algorithm Theoretical Basis Document, Tech. rep., NASA Earth Surface Mineral Dust Source Investigation (EMIT), https://github.com/emit-sds/emit-sds-tgp/blob/develop/docs/EMIT_L2B_TRACE_GAS_ATBD.md, accessed: 2026-03-17, 2026.

Carrascal, M. D., Puigcerver, M., and Puig, P.: Sensitivity of Gaussian plume model to dispersion specifications, Theoretical and Applied Climatology, 48, 147–157, https://doi.org/10.1007/BF00864921, 1993.

Chlus, A. M., Brodrick, P. G., Thorpe, A. K., Chapman, J. W., Jensen, D. J., Coleman, R. W., Fahlen, J., Olson-Duvall, W., Thompson, D. R., and Green, R. O.: AVIRIS-3 L2B Greenhouse Gas Enhancements, Facility Instrument Collection, ORNL Distributed Active Archive Center, https://doi.org/10.3334/ORNLDAAC/2358, accessed: 2026-03-17, 2024.

Coleman, R. W., Thorpe, A. K., Brodrick, P. G., Chlus, A., Fahlen, J. E., Bue, B., Chapman, J., Eckert, R. F., Jensen, D. J., Eastwood, M. L., Thompson, D. R., Elder, C. D., Beltran, S. G., Amezquita, D. R., Hopkins, F., and Green, R. O.: Identifying and quantifying greenhouse gas emissions with the AVIRIS-3 airborne imaging spectrometer, Remote Sensing of Environment, 332, 115 058, https://doi.org/https://doi.org/10.1016/j.rse.2025.115058, 2026.

Cusworth, D. H., Duren, R. M., Ayasse, A. K., Jiorle, R., Howell, K., Aubrey, A., Green, R. O., Eastwood, M. L., Chapman, J. W., Thorpe, A. K., Heckler, J., Asner, G. P., Smith, M. L., Thoma, E., Krause, M. J., Heins, D., and Thorneloe, S.: Quantifying methane emissions from United States landfills, Science, 383, 1499–1504, https://doi.org/10.1126/science.adi7735, 2024.

Dowell, D. C., Alexander, C. R., James, E. P., Weygandt, S. S., Benjamin, S. G., Manikin, G. S., Blake, B. T., Brown, J. M., Olson, J. B., Hu, M., Smirnova, T. G., Ladwig, T., Kenyon, J. S., Ahmadov, R., Turner, D. D., Duda, J. D., and Alcott, T. I.: The High-Resolution Rapid Refresh (HRRR): An Hourly Updating Convection-Allowing Forecast Model. Part I: Motivation and System Description, Weather and Forecasting, 37, 1371–1395, https://doi.org/10.1175/waf-d-21-0151.1, 2022.

Duren, R., Cusworth, D., Ayasse, A., Howell, K., Diamond, A., Scarpelli, T., Kim, J., O'neill, K., Lai-Norling, J., Thorpe, A., Zandbergen, S. R., Shaw, L., Keremedjiev, M., Guido, J., Giuliano, P., Goldstein, M., Nallapu, R., Barentsen, G., Thompson, D. R., Roth, K., Jensen, D., Eastwood, M., Reuland, F., Adams, T., Brandt, A., Kort, E. A., Mason, J., and Green, R. O.: The Carbon Mapper emissions monitoring system, Atmospheric Measurement Techniques, 18, 6933–6958, https://doi.org/10.5194/amt-18-6933-2025, 2025.

Duren, R. M., Thorpe, A. K., Foster, K. T., Rafiq, T., Hopkins, F. M., Yadav, V., Bue, B. D., Thompson, D. R., Conley, S., Colombi, N. K., et al.: California's methane super-emitters, Nature, 575, 180–184, 2019.

Eastwood, M. L., Thompson, D. R., Green, R. O., Fahlen, J. E., Adams, T. J., Brandt, A. R., Brodrick, P. G., Chlus, A., Kort, E. A., Reuland, F., and Thorpe, A. K.: Direct measurement of plume velocity to characterize point source emissions, Proceedings of the National Academy of Sciences, 122, e2507350 122, https://doi.org/10.1073/pnas.2507350122, 2025.

https://doi.org/10.5194/egusphere-2026-3771
Preprint. Discussion started: 27 July 2026

El Abbadi, S. H., Chen, Z., Burdeau, P. M., Rutherford, J. S., Chen, Y., Zhang, Z., Sherwin, E. D., and Brandt, A. R.: Technological maturity of aircraft-based methane sensing for greenhouse gas mitigation, Environmental Science & Technology, 58, 9591–9600, 2024.

Fahlen, J. E., Brodrick, P. G., Coleman, R. W., Elder, C. D., Thompson, D. R., Thorpe, A. K., Green, R. O., Green, J. J., Lopez, A. M., and Xiang, C.: Sensitivity and Uncertainty in Matched-Filter-Based Gas Detection With Imaging Spectroscopy, IEEE Transactions on Geoscience and Remote Sensing, 62, 1–10, https://doi.org/10.1109/TGRS.2024.3440174, 2024.

Gałkowski, M., Marshall, J., Fuentes Andrade, B., and Gerbig, C.: Impact of atmospheric turbulence on the accuracy of point source emission estimates using satellite imagery, Atmospheric Chemistry and Physics, 25, 13 831–13 848, https://doi.org/10.5194/acp-25-13831-2025, 2025.

Green, R. O., Mahowald, N., Thompson, D. R., Ung, C., Brodrick, P., Pollock, R., Bennett, M., Lundeen, S., Joyce, M., Olson-Duvall, W., Oaida, B., Bradley, C., Diaz, E., Clark, R., Vannan, S., Swayze, G., Kokaly, R., Ginoux, P., Miller, R., Okin, G., Garcia-Pando, C. P., Ehlmann, B., Kalashnikova, O., Painter, T. H., Realmuto, V., Chadwick, D., Ben-Dor, E., Pearlshtien, D. H., Guanter, L., Phillips, B., Reath, K., Thorpe, A., Shaw, L., Keebler, A., Ochoa, F., Grant, K., Sen, A., Duren, R., Obiso, V., Gonçalves-Ageitos, M., and Huang, Y.: Performance and Early Results from the Earth Surface Mineral Dust Source Investigation (EMIT) Imaging Spectroscopy Mission, in: 2023 IEEE Aerospace Conference, pp. 1–10, https://doi.org/10.1109/AERO55745.2023.10115851, 2023.

Guanter, L., Irakulis-Loitxate, I., Gorroño, J., Sánchez-García, E., Cusworth, D. H., Varon, D. J., Cogliati, S., and Colombo, R.: Mapping methane point emissions with the PRISMA spaceborne imaging spectrometer, Remote Sensing of Environment, 265, 112 671, https://doi.org/https://doi.org/10.1016/j.rse.2021.112671, 2021.

Hersbach, H., Bell, B., Berrisford, P., Hirahara, S., Horányi, A., Muñoz-Sabater, J., Nicolas, J., Peubey, C., Radu, R., Schepers, D., Simmons, A., Soci, C., Abdalla, S., Abellan, X., Balsamo, G., Bechtold, P., Biavati, G., Bidlot, J., Bonavita, M., De Chiara, G., Dahlgren, P., Dee, D., Diamantakis, M., Dragani, R., Flemming, J., Forbes, R., Fuentes, M., Geer, A., Haimberger, L., Healy, S., Hogan, R. J., Hólm, E., Janisková, M., Keeley, S., Laloyaux, P., Lopez, P., Lupu, C., Radnoti, G., de Rosnay, P., Rozum, I., Vamborg, F., Villaume, S., and Thépaut, J.-N.: The ERA5 global reanalysis, Quarterly Journal of the Royal Meteorological Society, 146, 1999–2049, https://doi.org/https://doi.org/10.1002/qj.3803, 2020.

Irakulis-Loitxate, I., Guanter, L., Liu, Y.-N., Varon, D. J., Maasakkers, J. D., Zhang, Y., Chulakadabba, A., Wofsy, S. C., Thorpe, A. K., Duren, R. M., Frankenberg, C., Lyon, D. R., Hmiel, B., Cusworth, D. H., Zhang, Y., Segl, K., Gorroño, J., Sánchez-García, E., Sulprizio, M. P., Cao, K., Zhu, H., Liang, J., Li, X., Aben, I., and Jacob, D. J.: Satellite-based survey of extreme methane emissions in the Permian basin, Science Advances, 7, eabf4507, https://doi.org/10.1126/sciadv.abf4507, 2021.

Kim, J., Cusworth, D. H., Ayasse, A. K., Howell, K., O'Neill, K., and Duren, R. M.: Performance of Airborne Imaging Spectrometers for Carbon Dioxide Detection and Emission Quantification, Journal of Geophysical Research: Atmospheres, 130, e2024JD042 755, https://doi.org/https://doi.org/10.1029/2024JD042755, e2024JD042755 2024JD042755, 2025.

Krings, T., Gerilowski, K., Buchwitz, M., Reuter, M., Tretner, A., Erzinger, J., Heinze, D., Pflüger, U., Burrows, J. P., and Bovensmann, H.: MAMAP – a new spectrometer system for column-averaged methane and carbon dioxide observations from aircraft: retrieval algorithm and first inversions for point source emission rates, Atmospheric Measurement Techniques, 4, 1735–1758, https://doi.org/10.5194/amt-4-1735-2011, 2011.

Kuhlmann, G., Koene, E., Meier, S., Santaren, D., Broquet, G., Chevallier, F., Hakkarainen, J., Nurmela, J., Amorós, L., Tamminen, J., and Brunner, D.: The *ddeq* Python library for point source quantification from remote sensing images (version 1.0), Geoscientific Model Development, 17, 4773–4789, https://doi.org/10.5194/gmd-17-4773-2024, 2024.

https://doi.org/10.5194/egusphere-2026-3771
Preprint. Discussion started: 27 July 2026

Li, F., Lin, K., Yan, Y., Bai, S., Huang, Q., Feng, C., Sun, S., Zhao, S., Zhou, W., Zhou, C., Lin, J., Zhang, X., and Zhang, Y.: Comparing the performance of different hyperspectral satellite imaging spectroscopy in mapping methane point-source emissions, Remote Sensing of Environment, 334, 115 224, https://doi.org/https://doi.org/10.1016/j.rse.2025.115224, 2026.

Maasakkers, J. D., Varon, D. J., Elfarsdóttir, A., McKeever, J., Jervis, D., Mahapatra, G., Pandey, S., Lorente, A., Borsdorff, T., Foorthuis, L. R., Schuit, B. J., Tol, P., van Kempen, T. A., van Hees, R., and Aben, I.: Using satellites to uncover large methane emissions from landfills, Science Advances, 8, eabn9683, https://doi.org/10.1126/sciadv.abn9683, 2022.

Marjani, M., Mohammadimanesh, F., Varon, D. J., Radman, A., and Mahdianpari, M.: PRISMethaNet: A novel deep learning model for landfill methane detection using PRISMA satellite data, ISPRS Journal of Photogrammetry and Remote Sensing, 218, 802–818, https://doi.org/https://doi.org/10.1016/j.isprsjprs.2024.10.003, 2024.

Nassar, R., Mastrogiacomo, J.-P., Bateman-Hemphill, W., McCracken, C., MacDonald, C. G., Hill, T., O'Dell, C. W., Kiel, M., and Crisp, D.: Advances in quantifying power plant CO2 emissions with OCO-2, Remote Sensing of Environment, 264, 112 579, 2021.

Pang, Y., Tian, L., Hu, D., Gao, S., and Liu, G.: Separating and quantifying facility-level methane emissions with overlapping plumes for spaceborne methane monitoring, Atmospheric Measurement Techniques, 18, 455–470, https://doi.org/10.5194/amt-18-455-2025, 2025.

Roger, J., Irakulis-Loitxate, I., Valverde, A., Gorroño, J., Chabrillat, S., Brell, M., and Guanter, L.: High-Resolution Methane Mapping With the EnMAP Satellite Imaging Spectroscopy Mission, IEEE Transactions on Geoscience and Remote Sensing, 62, 1–12, https://doi.org/10.1109/TGRS.2024.3352403, 2024.

Sánchez-García, E., Gorroño, J., Irakulis-Loitxate, I., Varon, D. J., and Guanter, L.: Mapping methane plumes at very high spatial resolution with the WorldView-3 satellite, Atmospheric Measurement Techniques, 15, 1657–1674, https://doi.org/10.5194/amt-15-1657-2022, 2022.

Seinfeld, J. H. and Pandis, S. N.: Atmospheric chemistry and physics: from air pollution to climate change, John Wiley & Sons, 2016.

Shah, A., Allen, G., Pitt, J. R., Ricketts, H., Williams, P. I., Helmore, J., Finlayson, A., Robinson, R., Kabbabe, K., Hollingsworth, P., et al.: A near-field Gaussian plume inversion flux quantification method, applied to unmanned aerial vehicle sampling, Atmosphere, 10, 396, 2019.

Thompson, D., Thorpe, A., Frankenberg, C., Green, R., Duren, R., Guanter, L., Hollstein, A., Middleton, E., Ong, L., and Ungar, S.: Space-based remote imaging spectroscopy of the Aliso Canyon CH4 superemitter, Geophysical Research Letters, 43, 6571–6578, 2016.

Thompson, D. R., Leifer, I., Bovensmann, H., Eastwood, M., Fladeland, M., Frankenberg, C., Gerilowski, K., Green, R. O., Kratwurst, S., Krings, T., Luna, B., and Thorpe, A. K.: Real-time remote detection and measurement for airborne imaging spectroscopy: a case study with methane, Atmospheric Measurement Techniques, 8, 4383–4397, https://doi.org/10.5194/amt-8-4383-2015, 2015.

Thorpe, A., Brodrick, P., Chadwick, D., Lopez, A., Villanueva-Weeks, C., Fahlen, J., Jensen, D., Bender, H., Vinckier, Q., Xiang, C., Olson-Duvall, W., Chlus, A., Lundeen, S., Thompson, D., and Green, R.: EMIT L2B Methane Enhancement Data 60 m V002, NASA Land Processes Distributed Active Archive Center, https://doi.org/10.5067/EMIT/EMITL2BCH4ENH.002, accessed: 2026-03-17, 2025.

Thorpe, A. K., Roberts, D. A., Bradley, E. S., Funk, C. C., Dennison, P. E., and Leifer, I.: High resolution mapping of methane emissions from marine and terrestrial sources using a Cluster-Tuned Matched Filter technique and imaging spectrometry, Remote Sensing of Environment, 134, 305–318, https://doi.org/https://doi.org/10.1016/j.rse.2013.03.018, 2013.

Thorpe, A. K., Frankenberg, C., Thompson, D. R., Duren, R. M., Aubrey, A. D., Bue, B. D., Green, R. O., Gerilowski, K., Krings, T., Borchardt, J., Kort, E. A., Sweeney, C., Conley, S., Roberts, D. A., and Dennison, P. E.: Airborne DOAS retrievals of methane, carbon dioxide, and water vapor concentrations at high spatial resolution: application to AVIRIS-NG, Atmospheric Measurement Techniques, 10, 3833–3850, https://doi.org/10.5194/amt-10-3833-2017, 2017.

https://doi.org/10.5194/egusphere-2026-3771
Preprint. Discussion started: 27 July 2026

Thorpe, A. K., O'Handley, C., Emmitt, G. D., DeCola, P. L., Hopkins, F. M., Yadav, V., Guha, A., Newman, S., Herner, J. D., Falk, M., and Duren, R. M.: Improved methane emission estimates using AVIRIS-NG and an Airborne Doppler Wind Lidar, Remote Sensing of Environment, 266, 112 681, https://doi.org/https://doi.org/10.1016/j.rse.2021.112681, 2021.

Thorpe, A. K., Green, R. O., Thompson, D. R., Brodrick, P. G., Chapman, J. W., Elder, C. D., Irakulis-Loitxate, I., Cusworth, D. H., Ayasse, A. K., Duren, R. M., Frankenberg, C., Guanter, L., Worden, J. R., Dennison, P. E., Roberts, D. A., Chadwick, K. D., Eastwood, M. L., Fahlen, J. E., and Miller, C. E.: Attribution of individual methane and carbon dioxide emission sources using EMIT observations from space, Science Advances, 9, eadh2391, https://doi.org/10.1126/sciadv.adh2391, 2023.

Van Trees, H. L.: Detection, estimation, and modulation theory, part I: detection, estimation, and linear modulation theory, John Wiley & Sons, 2004.

Varon, D. J., Jacob, D. J., McKeever, J., Jervis, D., Durak, B. O. A., Xia, Y., and Huang, Y.: Quantifying methane point sources from fine-scale satellite observations of atmospheric methane plumes, Atmospheric Measurement Techniques, 11, 5673–5686, https://doi.org/10.5194/amt-11-5673-2018, 2018.

Varon, D. J., Jacob, D. J., Jervis, D., and McKeever, J.: Quantifying Time-Averaged Methane Emissions from Individual Coal Mine Vents with GHGSat-D Satellite Observations, Environmental Science & Technology, 54, 10 246–10 253, https://doi.org/10.1021/acs.est.0c01213, pMID: 32672947, 2020.

Zhang, X., Maasakkers, J. D., Roger, J., Guanter, L., Sharma, S., Lama, S., Tol, P., Varon, D. J., Cusworth, D. H., Howell, K., Thorpe, A. K., Brodrick, P. G., and Aben, I.: Global Identification of Solid Waste Methane Super Emitters Using Hyperspectral Satellites, Environmental Science & Technology, 59, 18 134–18 145, https://doi.org/10.1021/acs.est.4c14196, pMID: 40827757, 2025.